ACS central science

Research Article

http://pubs.acs.org/journal/acscii

Computationally-Guided Synthetic Control over Pore Size in Isostructural Porous Organic Cages

Anna G. Slater,[†,‡] Paul S. Reiss,[†,‡] Angeles Pulido,[§] Marc A. Little,[†] Daniel L. Holden,[†] Linjiang Chen,[†] Samantha Y. Chong,[†] Ben M. Alston,[†] Rob Clowes,[†] Maciej Haranczyk,[∥] Michael E. Briggs,[†] Tom Hasell,[†] Graeme M. Day,[*,§] and Andrew I. Cooper[*,†]

[†]Department of Chemistry and Materials Innovation Factory, University of Liverpool, Crown Street, Liverpool L69 7ZD, United Kingdom

[§]School of Chemistry, University of Southampton, Highfield, Southampton SO17 1BJ, United Kingdom

[∥]Computational Research Division, Lawrence Berkeley National Laboratory, Berkeley, California 94720, United States

Supporting Information

ABSTRACT: The physical properties of 3-D porous solids are defined by their molecular geometry. Hence, precise control of pore size, pore shape, and pore connectivity are needed to tailor them for specific applications. However, for porous molecular crystals, the modification of pore size by adding pore-blocking groups can also affect crystal packing in an unpredictable way. This precludes strategies adopted for isoreticular metal−organic frameworks, where addition of a small group, such as a methyl group, does not affect the basic framework topology. Here, we narrow the pore size of a cage molecule, **CC3**, in a systematic way by introducing methyl groups into the cage windows. Computational crystal structure prediction was used to anticipate the packing preferences of two homochiral methylated cages, **CC14**-*R* and **CC15**-*R*, and to assess the structure−energy landscape of a **CC15**-*R*/**CC3**-*S* cocrystal, designed such that both component cages could be directed to pack with a 3-D, interconnected pore structure. The experimental gas sorption properties of these three cage systems agree well with physical properties predicted by computational energy−structure−function maps.

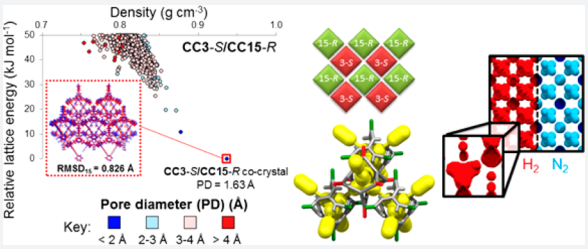

INTRODUCTION

There has been much interest recently in porous materials based on discrete organic molecules[1−4] such as porous organic cages (POCs).[5−9] Counter to expectations, these materials are now beginning to rival extended bonded frameworks, such as metal−organic frameworks (MOFs),[10] covalent−organic frameworks (COFs),[11] and organic polymer networks.[12] For example, the apparent Brunauer−Emmett−Teller surface area (SA_{BET}) achieved in molecular solids has reached remarkably high values of up to 3758 $m^2\ g^{-1}$.[8] Porous molecular materials have certain unique advantages: for example, unlike extended frameworks, they can be processed directly in solution to produce composite membranes.[13] The properties of these molecular materials can also be varied in a modular way by forming porous cocrystals that contain more than one molecule[14,15] and by using specific solvents to direct cage molecules into particularly useful crystal packings.[16,17]

CC3-*R* is a homochiral POC with four triangular windows that crystallizes with a 3-D diamondoid pore topology. This porous structure, **CC3***α*, has been well-studied, both experimentally and computationally, and shape- and size-selective molecular separations have been demonstrated.[18−20] The ability to tailor the pore channel size in **CC3** is an attractive target because this could enable new or more selective separations. For instance, narrowing of the pore window size in **CC3** might allow selectivity for small guests, such as hydrogen (H_2), deuterium (D_2), and tritium (T_2), which diffuse unimpeded through the pore network of unmodified **CC3***α*. Traditional molecular sieving is impractical for the separation of isotopes, but kinetic quantum sieving is possible at low temperatures in materials with sufficiently narrow pore diameters (PD) of less than 0.7 nm.[21] Zeolites,[22] porous carbons,[23] and metal−organic frameworks[24] have been shown to have selectivity for D_2 over H_2; achieving D_2/H_2 selectivity with a solution-processable porous molecular material could lead to new isotope separation membranes. We therefore targeted POCs with smaller pores than **CC3***α*, but with retention of the same 3-D diamondoid pore topology.

The use of methyl groups to reduce pore size has been reported previously for both MOFs and COFs.[25−27] Mastalerz *et al.* also reported a series of O-alkylated [4 + 6] cages with different cavity sizes, but the crystal packing of the O-methylated cage was found to be different from that of the unmethylated cage, and the other four alkylated analogues were not sufficiently crystalline to allow structure determination.[28] This highlights the significant difficulty in controlling the pore size of organic cages in an "isoreticular" manner. Small changes

Received: April 7, 2017

DOI: 10.1021/acscentsci.7b00145
ACS Cent. Sci. XXXX, XXX, XXX−XXX

to the cage building blocks will often result in significant changes to the solid-state crystal packing, thwarting attempts to produce isoreticular series of POCs, as observed with the four imine POCs, **CC1**−**CC4**.[29,30] This sensitivity of crystal packing to molecular functionality is a central challenge in molecular crystal engineering, extending beyond the specific example of porous molecular solids.

Here, we report a computationally guided strategy for fine-tuning the pore size in crystalline POC materials. Our approach involves the addition of methyl groups to a parent cage, **CC3**-*R*. Two methylated TFB precursors, 1,3,5-trimethyl-2,4,6-tris-(formyl)benzene (Me_3TFB) and 1,3,5-triacetylbenzene (TAB), were used to form these **CC3**-*R* analogues, referred to here as **CC14**-*R* and **CC15**-*R*, respectively (Scheme 1). In **CC14**-*R* and **CC15**-*R*, the methyl groups narrow the dimension of the triangular cage windows compared to the parent cage, **CC3**-*R*. Since crystal packing for molecules is known to be sensitive to such small modifications, we used crystal structure prediction (CSP) to investigate the packing preferences of the cages. **CC14**-*R* was predicted to pack isostructurally with **CC3**α, while polymorphism was predicted to be likely for **CC15**-*R* because of the absence of a strongly preferred, low-energy packing motif. To overcome the lack of a stable diamondoid porous packing for **CC15**-*R*, CSP was used to investigate cocrystallization of **CC15**-*R* with **CC3**-*S*; these calculations showed that the desired diamondoid pore network is the most stable packing for the heterochiral, quasiracemic cocrystal. The CSP landscapes were then transformed into energy−structure−function (ESF) maps of pore size for the static predicted crystal structures. To account for the effects on porosity of thermal fluctuations, including flexibility of the molecular geometry, molecular dynamics (MD) simulations were used to calculate the pore size reduction in the methylated systems. All predictions were confirmed experimentally, illustrating that computational guidance allows us to target and access porous organic crystals with systematic control over pore size.

DISCUSSION

Synthesis of Methylated CC3 Derivatives. We initially screened cage-forming reactions with methylated TFB precursors to determine whether **CC3**-*R* analogues could be synthesized. Me_3TFB (Scheme 1) was synthesized from 1,3,5-trimethyl-2,4,6-tris(bromomethyl)benzene via a modified Hass procedure.[31] Despite screening various conditions, a **CC3** derivative containing four Me_3TFB units per cage, an initial target of this study, could not be synthesized. This is most likely due to the steric hindrance of the methyl groups inhibiting the formation of a closed cage structure. Hence, different ratios of Me_3TFB and TFB were reacted with (*R*,*R*)-1,2-cyclohexanediamine (*R*,*R*-CHDA), and the product distribution was analyzed by analytical high-performance liquid chromatography (HPLC). We showed previously that mixtures of POC molecules can be prepared by scrambling two vicinal diamines into the vertex positions of the cage.[32,33] In those previous studies, all seven hypothetical scrambled cage species were obtained. By contrast, only two cage species were observed here—**CC3**-*R* and **CC14**-*R*, which has one Me_3TFB unit per cage—irrespective of the ratio of the two trialdehydes (Table S1 and Figure S1). **CC14**-*R* was isolated from this mixture of **CC3**-*R* and **CC14**-*R*

Scheme 1. Synthesis and Schematic Representation of Cage Molecules CC3-*R*, CC14-*R*, and CC15-*R*[a]

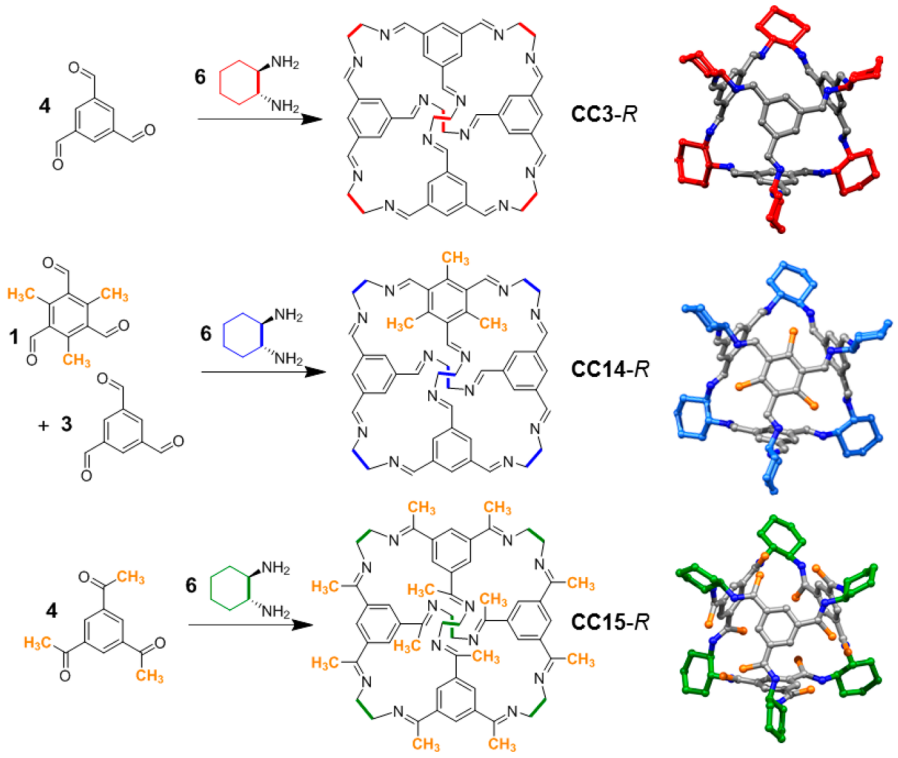

[a]The *S*-enantiomer would be formed from *S*,*S*-CHDA (not shown). In **CC14**-*R*, three of the four cage windows are partially occluded by a single methyl group per window (highlighted in orange), whereas in **CC15**-*R*, all four cage windows are partially occluded by three methyl groups per window (highlighted in yellow). Hydrogen atoms omitted for clarity.

DOI: 10.1021/acscentsci.7b00145
ACS Cent. Sci. XXXX, XXX, XXX−XXX

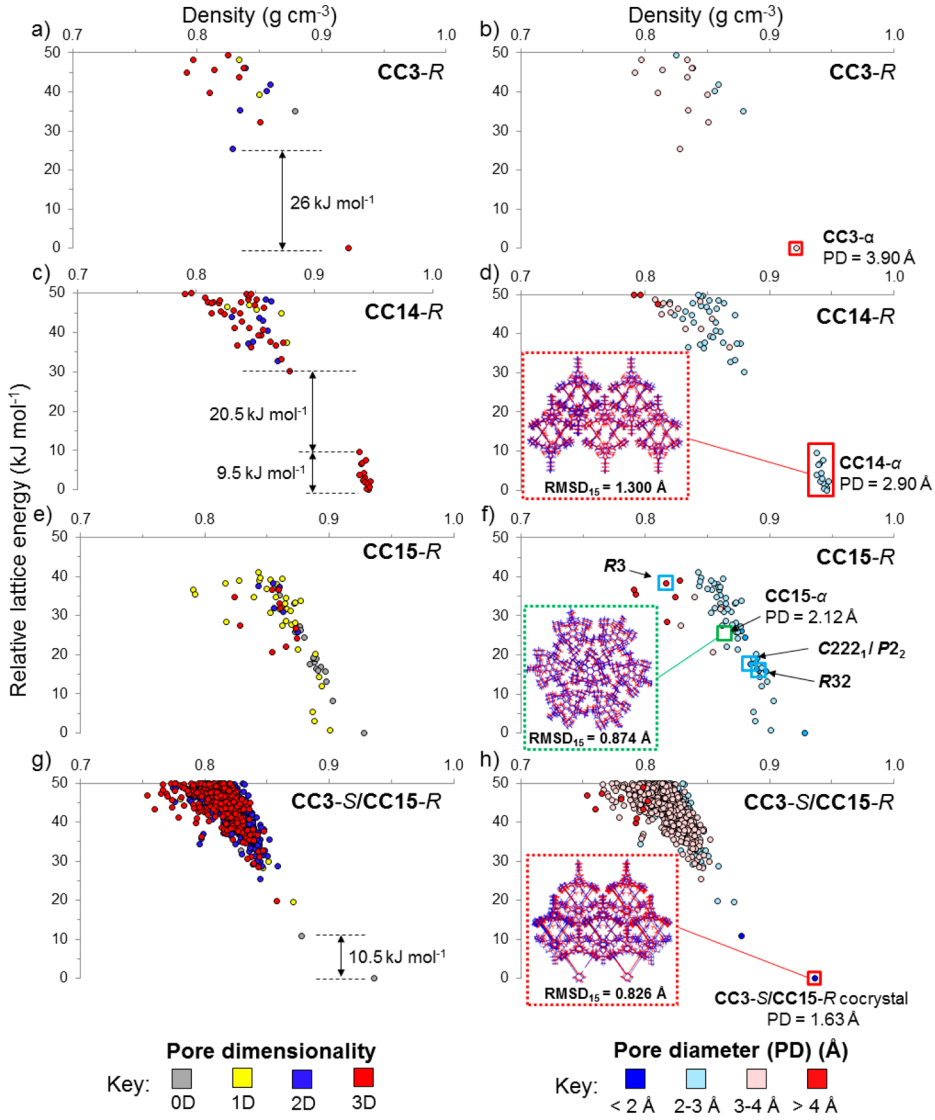

Figure 1. Energy–structure–function (ESF) maps for (a, b) **CC3**, (c, d) **CC14**-*R*, (e, f) **CC15**-*R*, and (g, h) the **CC3**-*S*/**CC15**-*R* cocrystal. Each point corresponds to a predicted crystal structure, color-coded by a calculated physical property. The symbols are color coded by (a, c, e, g) pore channel dimensionality, assessed using a H_2 probe radius (1.09 Å) or (b, d, f, h) calculated pore diameter (PD). Despite having the desired window-to-window packing, the low energy predicted structures for the **CC3**-*S*/**CC15**-*R* cocrystals are 0-D (nonporous) because the methyl groups occlude the pore to hydrogen, at least in the static crystal structure. All isolated, desolvated polymorphs that possess a diamondoid network are highlighted by a red square. For **CC15**-*R* (f), the green square highlights where the desolvated experimental structure would place on the landscape, while the blue squares highlight **CC15**-*R* structures that were observed experimentally as solvates (**c**). Insets show the overlay of molecular packing in experimentally determined (red) and calculated (blue) structures. $RMSD_{15}$ is the root mean squared deviation in atomic positions in the best overlay of a cluster of 15 molecules from the calculated and experimental structures, ignoring hydrogen atoms and disordered methyl groups for **CC14**. PD labeled on plots b, d, f, and h is the calculated pore diameter.

in high purity using preparative HPLC (>99% a/a by HPLC; Figures S2–S7).

To further occlude the cage windows, the methyl groups can be located on the imine such that they protrude further into the cage window. This was achieved by reacting TAB with *R*,*R*-CHDA to afford **CC15**-*R*, a **CC3**-*R* analogue with 12 methyl groups appended to the imine functionalities (Scheme 1, Figures S8–S11).

Crystal Structure Prediction and Energy–Structure–Function Maps. Crystal structure prediction (CSP) methods can determine the stable arrangements that are available to a molecule during crystallization, as usually presented in plots of lattice energy versus crystal density or volume. The probability of a given structural arrangement being stable and experimentally accessible relates to its predicted lattice energy. Specific physical properties for each of the predicted structures, such as pore dimensionality, pore size, gas uptakes, and gas selectivity, can also be calculated and projected onto CSP plots to create energy–structure–function (ESF) maps (Figure 1).[34]

Previously, we used CSP to investigate the crystal packing preference of homochiral **CC3**-*R*;[14] the global lattice energy minimum predicted structure is the observed **CC3***α* packing and is separated from the rest of the predicted structures by a large energy gap (Figure 1a,b), indicating a strong thermodynamic preference for **CC3**-*R* to crystallize as **CC3***α* (Figure 2e).[29] Here, we used an equivalent computational strategy to investigate the crystal packing preferences of **CC14**-*R* and **CC15**-*R*. Starting points for the molecular geometries

DOI: 10.1021/acscentsci.7b00145
ACS Cent. Sci. XXXX, XXX, XXX–XXX

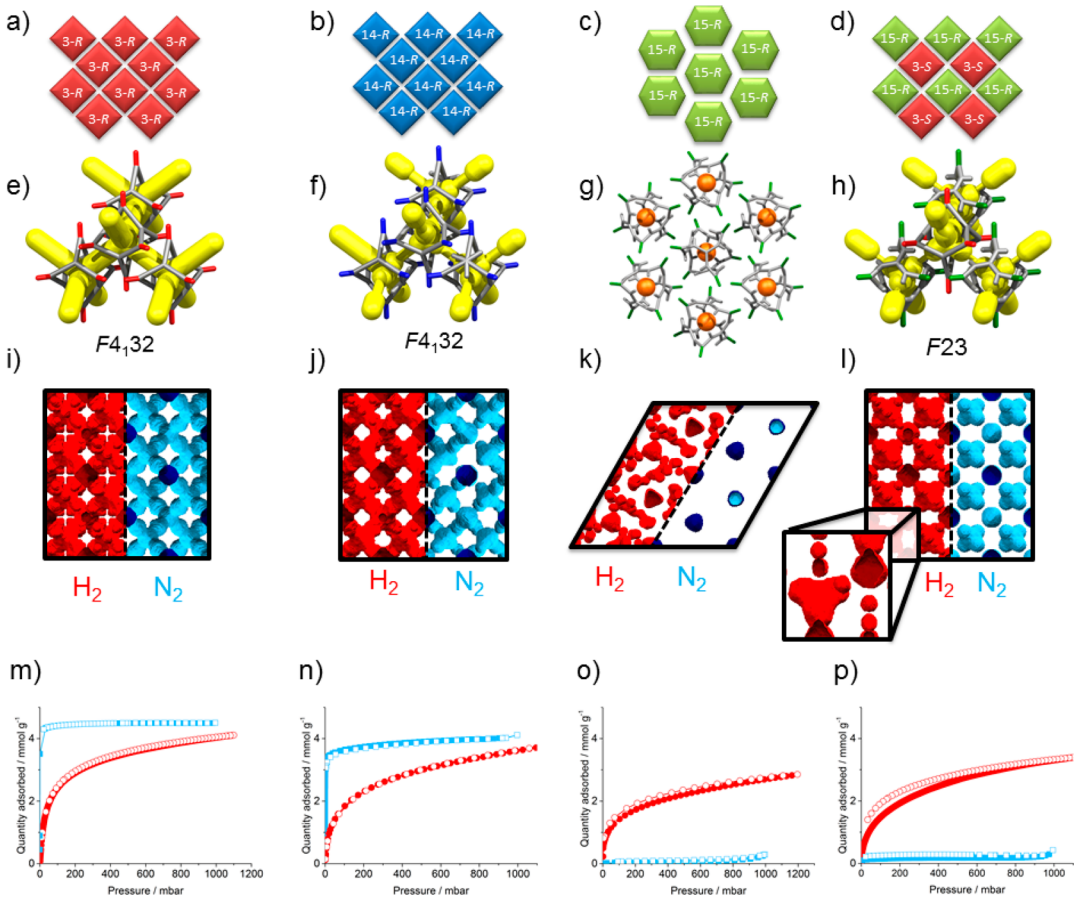

Figure 2. Crystal packing, pore topology, surface area plots, and sorption isotherms for homochiral **CC3***α*, **CC14***α*, **CC15***α*, and **CC3**-*S*/**CC15**-*R* cocrystal. (a–d) Simplified representation of the cage packing in **CC3***α*, **CC14***α*, **CC15***α*, and **CC3**-*S*/**CC15**-*R* cocrystal. (e–h) Simplified representation of the crystal structures of these cages, with pore channels shown in yellow. (i–l) Surface area plots, measured with two probe sizes: H_2 (red, 1.09 Å) and N_2 (blue, 1.7 Å). As more methyl groups are added to the structures (from left to right), the pores become narrower; in **CC15***α* and **CC3**-*S*/**CC15**-*R* cocrystal the cage cavities are occluded for a N_2 probe. These correlate well with the (m–p) hydrogen (red) and nitrogen (blue) sorption isotherms for **CC3***α*, **CC14***α*, **CC15***α*, and **CC3**-*S*/**CC15**-*R* cocrystal respectively at 77 K and 1 bar. Closed symbols show adsorption, and open symbols show desorption isotherms, respectively.

of **CC14**-*R* and **CC15**-*R* were obtained by adding methyl groups to the optimized gas phase geometry of **CC3**-*R*. The **CC14**-*R* and **CC15**-*R* isolated molecules were then geometry optimized using density functional theory (DFT) at the B3LYP/6-311G** level using the Gaussian09 software.[35] Molecular geometries were subsequently held rigid during crystal structure generation and lattice energy minimizations, which employed an anisotropic atom–atom potential using the DMACRYS software.[36]

In contrast to **CC3**-*R*, which has a unique predicted global minimum structure separated by 25.5 kJ mol^{-1} (Figure 1a,b), the lattice energy landscape of homochiral **CC14**-*R* shows a cluster of 14 structures, spread over an energy range of 9.5 kJ mol^{-1}, with a substantial gap of 20.5 kJ mol^{-1} between the top of this group and the rest of the energy landscape (Figure 1c,d). All 14 of these structures (Figure S12) exhibit window-to-window packing, and each possesses a diamondoid pore network that is isostructural with **CC3***α*. The methyl groups are ordered in each of the 14 structures, but their relative orientation varies between structures. The small energy range encompassing this group of structures suggests that there might be no strong preference for the position of the methyl groups in the crystal. Hence, **CC14**-*R* is predicted to form a diamondoid porous network, like **CC3***α*, where the cage molecules pack window-to-window, potentially with little preferential orientation and, thus, disorder of the methyl groups. That is, we can predict *a priori* that addition of three methyl groups to one aryl face of **CC3**-*R* should not disrupt its low energy packing mode.

For **CC15**-*R*, there are no large energy gaps between any of the low-energy predicted crystal structures (Figure 1e,f), quite unlike the landscapes for **CC3**-*R* (Figure 1a,b) and **CC14**-*R* (Figure 1c,d). Even without detailed analysis of the structures in the landscape, this suggests that **CC15**-*R* lacks a strongly favored packing mode and might have greater potential for polymorphism than either **CC3**-*R* or **CC14**-*R*. A search of this landscape shows that none of the predicted structures for **CC15**-*R* exhibit the desired diamondoid window-to-window packing up to at least 40 kJ mol^{-1} above the global minimum, which we estimate to be the energy window within which the CSP procedure used here has fully explored the range of possible structures. Therefore, window-to-window packing must be more than 40 kJ mol^{-1} less stable than the lowest energy predicted packing for this molecule. Rather than window-to-window packing, there is a predicted tendency for **CC15**-*R* to pack preferentially in a window-to-arene manner, which reduces pore connectivity in the crystal. To investigate the relative energy of the target diamondoid pore network,

DOI: 10.1021/acscentsci.7b00145
ACS Cent. Sci. XXXX, XXX, XXX–XXX

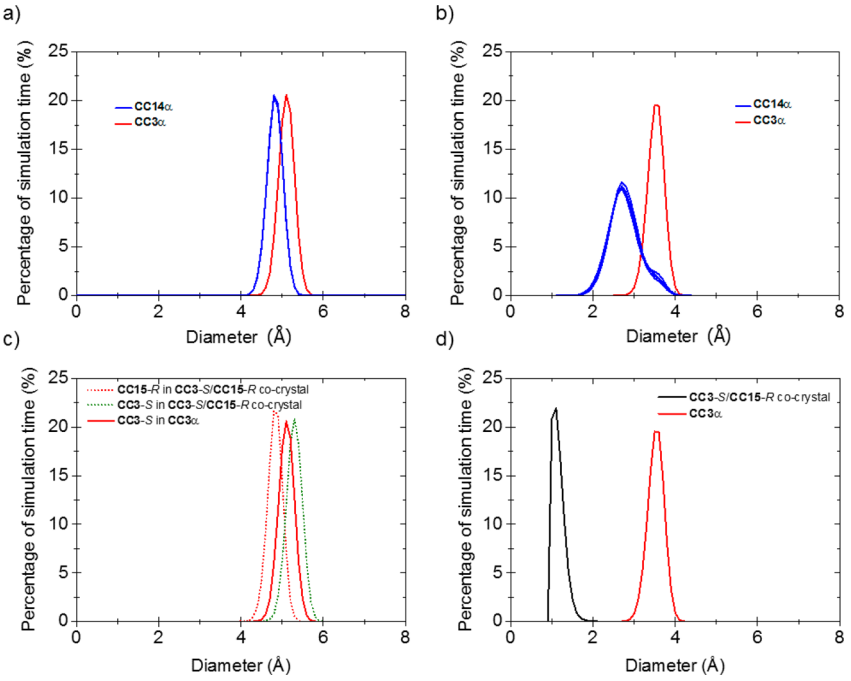

Figure 3. (a, b) Overlaid analysis for five different models of the **CC14***α* crystal structure showing (a) the cage cavity size and (b) PLE. The cage cavity size distribution and PLE calculated from molecular dynamics simulations at T = 300K. (c) Cage cavity size distribution and (d) PLE for the predicted **CC3**-*S*/**CC15**-*R* cocrystal. **CC3***α* is shown in red for comparison.

and to understand why it did not appear within the predicted structures, a computational model of **CC15**-*R* was built with the cages packed in the diamondoid window-to-window arrangement. Starting from the lowest energy predicted **CC3***α* structure, **CC3**-*R* molecules were replaced with **CC15**-*R* and the generated structure was lattice energy minimized at the same level of theory used in the CSP calculations. This resulting isostructural **CC15**-*R* model structure (Figure S14a) was predicted to be 99 kJ mol^{-1} above the CSP global energy minimum (Figure S15, black diamond) with a lattice energy of −120.8 kJ mol^{-1}. In this artificially produced structure, steric repulsion between the methyl groups forces the **CC15**-*R* molecules further apart (Figure S14), resulting in a much lower crystal density of 0.676 g cm^{-3} (Figures S14 and S15) compared to 0.922 g cm^{-3} for **CC3***α* (Table S2). Even allowing for solvent stabilization effects, which can stabilize lower-density crystal packings, these relative stabilities suggest that **CC15**-*R*, unlike **CC14**-*R*, should not form a phase that is isostructural with **CC3***α*.

Previous studies[14,15,29] have shown that preferential heterochiral window-to-window interactions between opposite handed cages can favor window-to-window crystal packings. To investigate whether **CC15**-*R* would benefit from the additional stabilization brought by cocrystallizing cages of opposite chirality, we built computational models of racemic **CC15** (**CC15**-*S*/**CC15**-*R*) and the quasiracemic **CC3**-S/**CC15**-*R* cocrystal, following a similar strategy used for the window-to-window **CC15**-*R* model. The racemic **CC15** structure was approximately 26 kJ mol^{-1} more stable than the corresponding homochiral **CC15** model (Table S2), but the overall relative stability was still 73 kJ mol^{-1} above the global minimum homochiral structure (Table S2 and Figure S15), and hence energetically disfavored. The extent of methylation in **CC15** seems to make a diamondoid, window-to-window packing mode unfavorable for both homochiral and racemic forms.

In principle, cocrystallization of **CC15**-*R* with a structurally related cage without methyl groups, such as **CC3**-*S*, might reduce the steric repulsion between adjacent cages enough to allow window-to-window packing, while still allowing the methyl groups in **CC15** to constrict the diamondoid pore dimensions. CSP was therefore used to investigate packing preferences of **CC3**-*S*/**CC15**-*R* (Figure 1g,h), assuming a 1:1 stoichiometry of **CC3**-*S* to **CC15**-*R*. The global lattice energy minimum predicted structure exhibits the desired **CC3**-S/**CC15**-*R* window-to-window arrangement (Figure 1h, red square) and was separated by 10.8 kJ mol^{-1} from the remainder of predicted structures. Hence, these calculations demonstrate that cocrystallization with **CC3** should accommodate the 12 additional methyl groups in **CC15**, restoring the energetic preference for the desired diamondoid pore network.

Pore dimensionality was calculated for each structure in the four systems, using a 1.09 Å hydrogen probe radius (Figure 1a,c,e,g). Both **CC3**-*R* and **CC14**-*R* show a high proportion of 3-D pore networks (Figure 1a,c filled red circles), whereas **CC15**-*R* exhibits a broader array of dimensionalities (Figure 1e, filled gray, yellow, blue, and red circles). The latter can be attributed to the additional methyl groups in **CC15**-*R*, which frustrate the window-to-window packing between cages, as discussed above. Cocrystallization of **CC15**-*R* with **CC3**-*S* increases the proportion of structures that possess a 3-D pore network (Figure 1g, filled red circles), although, unlike for **CC3**-*R* (Figure 1a) and **CC14**-*R* (Figure 1c), the global minimum structure is predicted to have 0-D porosity with respect to the probe radius, despite having the desired window-to-window packing. This is due to the methyl groups in **CC15**-*R*, which narrow the pore window size in the static crystal structure. This is also apparent in the respective ESF maps for pore diameter (Figure 1b,d,h), which predict that the pore diameter for the global minimum structure decreases, as denoted by the color-coding in these maps, in the isoreticular

DOI: 10.1021/acscentsci.7b00145
ACS Cent. Sci. XXXX, XXX, XXX−XXX

series **CC3**-*R* (Figure 1b, pink circle) to **CC14**-*R* (Figure 1d, light blue circles) to **CC3**-*S*/**CC15**-*R* (Figure 1h, dark blue circle). The trend in the pore diameter goes **CC3***α* (3.90 Å) > **CC14** (2.90 Å) > **CC3**-*S*/**CC15**-*R* cocrystal (1.63 Å), highlighting that the addition of methyl groups to the **CC3** core tunes pore size. Although there is a spread of low energy structures for **CC14**-*R* (Figure 1d), the pore diameters for these are all equivalent.

Crystallization of Methylated CC3 Derivatives. Vial-in-vial crystallization of **CC14**-*R* from dichloromethane (DCM)−acetone gave octahedral crystals that were characterized by single crystal X-ray diffraction (SCXRD). **CC14**-*R* crystallized in the chiral cubic space group $F4_132$. As predicted by CSP, **CC14**-*R* packs isostructurally with **CC3***α* to form **CC14***α* (Figures 1d, 2a,b,e,f, and 3a,b). In **CC14***α*, the cage has tetrahedral symmetry and packs window-to-window such that a diamondoid pore network passes though the cage windows. No ordering of the methyl groups between cages was apparent by experiment (Figures 2f and S16), again in keeping with the CSP landscape for **CC14**-*R* (Figure 1c,d). A bulk sample of **CC14***α* was prepared by layering acetone onto a solution of the cage in DCM, followed by slow evaporation under a flow of nitrogen. This bulk material was desolvated at 60 °C under vacuum, and PXRD analysis confirmed that the desolvated **CC14***α* matched the simulated powder pattern from the SCXRD (Figure S17).

A crystallization screen of **CC15**-*R* identified various solvates, but as suggested by the CSP, we were unable to isolate any material that possessed a **CC3***α*-like window-to-window packing. **CC15**-*R* crystallized from DCM−methanol in the trigonal space group *P*3 (with 3 independent molecules in the asymmetric unit, $Z' = 3$), where **CC15**-*R* packs window-to-arene along *c* (Figure S19), which was a common feature observed in the CSP data set. A single crystal of the *P*3 structure was thermally desolvated *in situ* to yield **CC15***α* (Figures 1f, 2c,g, and 3c,d). Desolvation was accompanied by a contraction in the cell volume (∼9% at 100 K, equating to a contraction of ∼206 Å^3 of the unit cell volume per **CC15**-*R*) because the window-to-arene stacks pack closer together along *a* and *b* (Figure S20). Three additional solvated crystal structures were obtained in the space groups $C222_1$, *R*32, and *R*3 (Figures S21−S25, Table S3), with the orthorhombic $C222_1$ phase observed to undergo a single-crystal to single-crystal transformation to monoclinic $P2_1$ upon thermal desolvation (Table S4). A single window-to-window interaction was evident in the $C222_1$ and $P2_1$ crystal structures, at a cage center to cage center separation distance of approximately 12 Å; this is approximately 1 Å longer than the comparable distance in **CC3***α*. Due to the absence of a preferential crystal packing motif, it proved difficult to obtain phase-pure samples for **CC15**-*R* on a large scale; again, this was suggested by the CSP landscape for this molecule (Figure 1e,f). Only the trigonal *P*3 crystalline phase of **CC15***α* could be isolated on a significant scale with sufficient phase purity. Desolvation of this bulk material at 100 °C for 12 h was carried out with no apparent loss of crystallinity (Figures S26 and S27), and the gas sorption properties of this desolvated material were investigated.

One current limitation of CSP is the huge computational expense of modeling high Z' structures, such as the *P*3, $Z' = 3$ polymorph, with three crystallographically distinct **CC15** cages in the asymmetric unit. Sampling the full structural space for such low symmetry structures is computationally unaffordable within a reasonable time scale for this size of molecule, so this structure was not within the predicted set. By contrast, three of the other experimental **CC15** solvates ($Z' = 1$) were found among the set of predicted structures in space groups *C*2 (*R*32 solvate), $P2_1$ ($P2_1$ and $C222_1$ solvates), and *P*1 (*R*3 solvate), with relative energies of 16, 18, and 38 kJ mol^{-1}, respectively, above the global minimum (Figure 1f, Table S2, and Figure S13). To calculate the relative stability of the observed experimental **CC15***α* polymorph ($Z' = 3$), a computational model was built from the desolvated SCXRD data. Using this model, **CC15***α* was found to be located 25 kJ mol^{-1} above the global minimum on the predicted **CC15**-*R* energy landscape (Figure 1f, green square), and hence it has comparable relative stability to the other observed **CC15**-*R* solvates. As such, the formation of all four of these solvate structures can be ascribed to stabilizing effect of the crystallization solvents.[29,34,37] A good geometric match was observed between the observed **CC15**-*R* solvate frameworks and the predicted structures (Figures 1f and S13).

We also attempted to crystallize **CC15**-*S* with **CC15**-*R* to see whether heterochiral cage pairings could direct window-to-window crystal packings, notwithstanding our calculations, above, which suggest that this should not succeed. When racemic **CC15** was crystallized from DCM−hexane or DCM−Et_2O, centrosymmetric $P\bar{1}$ and $P2_1/n$ crystal structures were isolated, respectively (Figures S29 and S30). As predicted, neither structure displayed the desired window-to-window packing mode. By contrast, the **CC3**-*S*/**CC15**-*R* cocrystal was successfully prepared by mixing a solution of **CC15**-*R* with an equimolar quantity of **CC3**-*S* in DCM. A homogeneous, clear solution was produced; this turned cloudy after standing for 1 h as crystallites were formed. Structure determination by SCXRD revealed the diamondoid **CC3**-*S*/**CC15**-*R* cocrystal had crystallized in the chiral cubic space group *F*23, which was the only polymorph isolated in these experiments. In agreement with the CSP global lattice energy minimum, the cage molecules pack window-to-window (Figure 1h), with each **CC3**-*S* cage surrounded by four **CC15**-*R* cages (Figures 2d,h and S31). PXRD analysis of the desolvated bulk material showed that it remained phase-pure and matched the simulated data from the single crystal structure (Figure S32).

Computational Investigation of Physical Properties. Computed ESF maps (Figure 1b,d,h) give us an *a priori* picture of the likely decrease in the pore diameter for the isoreticular series **CC3***α*−**CC14***α*−**CC3**-*S*/**CC15**-*R* cocrystal. However, these ESF maps are produced from static predicted crystal structures: they do not take account of the effect of lattice vibrations on pore dimensions and connectivity. In previous studies,[38−40] molecular dynamics (MD) simulations were used to understand the diffusivity of small gas molecules in **CC3***α* and to calculate a time-averaged, pore-limiting envelope (PLE), which accounts for molecular motion about the equilibrium crystal structure, as well as molecular flexibility and intramolecular vibrations. This PLE rationalizes the diffusion of gas molecules such as Kr, Xe, and SF_6, which have kinetic diameters that are larger than the pore diameter for **CC3***α*.[19,41] Here, we used MD calculations to evaluate the properties of our isoreticular series of cage cocrystals, and to investigate the effect of the methyl groups on both the cavity size and the PLE. For reasons of computational expense, these MD simulations were carried out for individual structures, but in principle this could be automated to produce dynamic PLE ESF maps, analogous to the static PD ESF maps shown in Figure 1b,d,f,h.

For **CC14**-*R*, the position of the methylated benzene is disordered with respect to adjacent cage molecules. MD simulations

DOI: 10.1021/acscentsci.7b00145
ACS Cent. Sci. XXXX, XXX, XXX−XXX

were therefore run for five structural models with the methylated benzene placement randomized to ensure that a statistical representation of different packing motifs was sampled. Analysis of the five simulated **CC14**-*R* structures showed that the cavity size distribution for all five models remained consistent, even though the position of the methylated benzene was randomized: this was confirmed by the visual pore size distribution plots (Figure S34). This resulted in a slightly reduced average cavity diameter of 4.80 Å (the peak of the cage size distribution), as compared with 5.10 Å in **CC3**-*R* (Figure 3a). As expected, the PLE of **CC14**-*R* was reduced, with the precise shape of the pore envelope determined by the relative positions of the methylated cage windows of adjacent cages in the five **CC14**-*R* simulations. This is reflected by the variation in intensity in the shoulder peak of the PLE for the different models (Figure 3b). The surface area plots (Figures 2j and S34) also show that the methyl groups in **CC14**-*R* have a direct impact on the interstitial void sites in the structure with respect to **CC3**. When compared to both homochiral and racemic **CC3***α*, the diameter of these interstitial sites in **CC14**-*R* is reduced from ∼2.50 Å to 1.5−2.0 Å. This creates a bottleneck in the structure, which could directly impact the diffusion kinetics of gases.

For the **CC3**-*S*/**CC15**-*R* cocrystal, the PLE is restricted by the three ordered methyl groups in each **CC15**-*R* window. These groups reduce the PLE dramatically, shifting the most probable window diameter from 3.60 Å (for **CC3**-*R*) to just 1.09 Å (Figure 3d). Thus, the N_2 surface area plot (Figure 2l) shows disconnected cage cavities. Taken alone, this would suggest that the cage window in this cocrystal is too small for any gas diffusion, even for H_2. However, the PLE was calculated using the empty, guest-free cage structure, which does not account for the possibility of cooperative diffusion.[42] Analysis of the cavity size distribution for the **CC3**-*S*/**CC15**-*R* cocrystal shows that there are two distinct cavity sites arising from the two different cages in the cocrystal (Figure 3c). Interestingly, the cavity size for **CC3**-*S* in the **CC3**-*S*/**CC15**-*R* cocrystal is smaller than it is in homochiral **CC3***α*, with an average diameter of 4.80 Å versus 5.10 Å in homochiral **CC3** (black vs red curves, respectively in Figure 3c). This is nearly identical to the cage cavity size in **CC14**-*R* (black curve, Figure 3a). **CC15**-*R* in this cocrystal has the largest internal cavity in this isoreticular cage series, with an average diameter of 5.30 Å (blue curve, Figure 3c).

Experimental Gas Sorption Properties. This isoreticular cage series allows us to evaluate the effect of pore size reduction on gas uptakes and diffusion kinetics (Figure 2m−p, Table 1). Nitrogen sorption measurements for **CC14***α* at 77 K and 1 bar displayed a type I isotherm, as rationalized by the crystal structure, which mirrors the isotherm shape of **CC3***α* (Figures 2m,n and S35). The overall nitrogen uptake and apparent BET surface area for **CC14***α* (4.11 mmol g^{-1}, 320 m^2 g^{-1}) are slightly lower than for **CC3***α* (4.50 mmol g^{-1}, 409 m^2 g^{-1}).[38] This decrease in specific surface area and gas uptake can be explained by the reduction in pore volume associated with the introduction of the methyl groups and the accompanying increase in molecular mass of the cage: these also block off some of the pore channels (Figure 2j). The sorption properties of this material with respect to other gases (H_2, CO_2, Xe, Kr) followed a similar trend, with slightly lower uptakes than for **CC3***α* in each case (Figures S35 and S36). The pore-size distribution (PSD) of these two cages, measured using CO_2 as a probe gas (Figure S37), shows a moderate decrease in pore width after introduction of the methyl groups, as suggested by the predicted PLE plots (Figure 3a). **CC14***α* has a similar sorption selectivity to **CC3***α* for Xe over Kr.[19]

Nitrogen sorption measurements for **CC15***α* at 77 K and 1 bar showed very little gas uptake in comparison to **CC3***α*. This highlights that the 12 methyl groups on each cage affect both the crystal packing of **CC15***α* and accessibility to the intrinsic cage voids, effectively shutting out nitrogen from the pores at 77 K (Table 1 and Figure S38). By contrast, **CC15***α* adsorbs approximately half as much H_2 and CO_2 in comparison to **CC3***α*, illustrating both a degree of porosity to smaller gas molecules at 77 K and increased flexibility at higher temperatures, respectively (Figures S38 and S39).

Gas sorption isotherms for the **CC3**-*S*/**CC15**-*R* cocrystal showed it to be nonporous to nitrogen at 77 K (Figures 2p and S40), confirming that the three methyl groups in each **CC15**-*R* window narrow the pore network in the crystal substantially. This material was, however, porous to H_2 at 77 K (Figures 2p and S40), with only a slight reduction in uptake compared to **CC3***α*, attributable to the reduced pore volume and increased average cage mass. However, there was a notable hysteresis in the H_2 isotherm, most likely due to slower kinetics (Figure 2p). Despite its narrower pore channels, this structural analogue of **CC3***α* remains porous to CO_2 and Xe at higher temperatures (Figures S41 and S42), again illustrating the important role that molecular flexibility and cooperative diffusion plays in defining the properties of these porous materials and suggesting that the methyl groups in the windows act like a "saloon door" (Figures S43 and S44).[43] This would explain the observed xenon uptake (Xe diameter = 4.10 Å) in the cocrystal, albeit with a pronounced hysteresis on desorption that is not observed for the isostructural **CC3***α*, indicating slower kinetics (Figure S42). Controlling the diffusion of Xe through the cage crystals in this way might give practical advantages in terms of breakthrough separations, with relevance to the treatment of radioactive air streams.[44] Narrow pore structures, such as those found in the **CC3**-*S*/**CC15**-*R* cocrystal, could also hold promise for isotope separation by quantum sieving. We believe that the narrow-pore **CC3**-*S*/**CC15**-*R* cocrystal could have a potential for separating mixtures of H_2 and D_2, exploiting both kinetic and thermodynamic aspects of the quantum sieving effect (Figures S45 and S46).

CONCLUSIONS

The methylation of TFB was chosen as a strategy to narrow the dimensions of the windows in analogues of the porous organic

Table 1. Comparison of the Gas Uptakes at 1 bar for CC3*α*, CC14*α*, CC15*α*, and CC3-*S*/CC15-*R* Cocrystal

	77 K			273 K		
	SA_{BET} /m^2 g^{-1}	N_2 /mmol g^{-1}	H_2 /mmol g^{-1}	CO_2 /mmol g^{-1}	Xe/mmol g^{-1}	Kr/mmol g^{-1}
CC3*α*	409	4.50	5.00	2.01	2.60	1.52
CC14*α*	320	4.11	3.64	1.57	1.61	0.96
CC15*α*	2.7	0.29	2.85	1.30	1.14	0.81
CC3-*S*/**CC15**-*R* cocrystal	13.1	0.43	3.39	1.84	1.25	0.79

DOI: 10.1021/acscentsci.7b00145
ACS Cent. Sci. XXXX, XXX, XXX−XXX

cage **CC3**, with the aim of inducing selectivity in the resultant porous materials. Two novel methylated organic cages, **CC14**-*R* and **CC15**-*R*, were prepared. CSP was used to investigate the effect on cage packing preferences that are induced by window methylation, and hence to guide the design of pore-narrowed isoreticular networks using ESF maps to visualize the impact on physical properties. In agreement with the CSP, **CC14**-*R* adopts the window-to-window packing analogous with **CC3**α, whereas **CC15**-*R* prefers to pack in a window-to-arene configuration, unless it is cocrystallized with a less bulky coformer, **CC3**-*S*. This illustrates the value of CSP in the design of functional materials: the introduction of methyl groups in **CC14**-*R* is innocuous with respect to diamondoid crystal packing whereas in **CC15**-*R* it is not, illustrating the limitations of intuitive crystal engineering strategies. The time scale for the single component CSP calculations (approximately 83,000 CPU hours, or 7 to 10 days in real time) is competitive with experimental time scales for synthesis and characterization of these materials, and this time scale is set to be reduced substantially as computational hardware and CSP methods evolve in the future. This should make it feasible, for example, to make routine *a priori* searches for more complex structures, such as those with multiple independent molecules including cocrystals and higher Z' structures, such as **CC15**α.

In the future, we envisage combined computational and experimental design strategies that build on these findings, such as investigating the potential effect of fluorination of the methyl groups. This could lead to a broader family of cages with tunable properties for specific applications. Our observations also raise the question of how to maintain selectivity while increasing the adsorption capacity of the material. One possible strategy is to adapt the principles demonstrated here for related molecules, such as **CC9** and **CC10**, where the vertex groups were chosen to direct molecular assembly and to create additional, extrinsic porosity.[45] Large extrinsic pores interconnected by narrow intrinsic pore bottlenecks could lead to high capacity materials with good adsorption/desorption kinetics and tunable guest selectivity.

■ ASSOCIATED CONTENT

Supporting Information

The Supporting Information is available free of charge on the ACS Publications website at DOI: 10.1021/acscentsci.7b00145.

Experimental details, CSP results, X-ray crystallography, MD simulations, and gas sorption (PDF)

■ AUTHOR INFORMATION

Corresponding Authors

*(A.I.C.) E-mail: aicooper@liverpool.ac.uk.
*(G.M.D.) E-mail: G.M.Day@soton.ac.uk.

ORCID

Samantha Y. Chong: 0000-0002-3095-875X
Andrew I. Cooper: 0000-0003-0201-1021

Author Contributions

‡A.G.S. and P.S.R. contributed equally to this work.

Notes

The authors declare no competing financial interest.

■ ACKNOWLEDGMENTS

We acknowledge the Engineering and Physical Sciences Research Council (EP/N004884/1) and European Research Council under the European Union's Seventh Framework Programme (FP/2007-2013) through Grant Agreement No. 321156 (ERC-AG-PE5-ROBOT) and 307358 (ERC-stG-2012-ANGLE) for funding. A.G.S. thanks the Royal Society for a Dorothy Hodgkin Fellowship. T.H. thanks the Royal Society for a University Research Fellowship. We thank Diamond Light Source for access to beamlines I19 (MT11231) and I11 (EE12336), which contributed to the work here. We thank the Advanced Light Source, supported by the Director, Office of Science, Office of Basic Energy Sciences, of the US Department of Energy under Contract No. DE-AC02-05CH11231, and S. J. Teat and K. J. Gagnon for their assistance. We acknowledge the ARCHER UK National Supercomputing Service via an EPSRC Programme Grant (EP/N004884), and the use of the IRIDIS High Performance Computing Facility, and associated support services at the University of Southampton, in the completion of this work. M.H. was supported by the Center for Applied Mathematics for Energy Related Applications (CAMERA) under contract no. DE-AC02-05CH11231.

■ REFERENCES

(1) Zhang, G.; Mastalerz, M. Organic Cage Compounds – from Shape-persistency to Function. *Chem. Soc. Rev.* **2014**, *43*, 1934–1947.
(2) Tian, J.; Thallapally, P. K.; McGrail, B. P. Porous Organic Molecular Materials. *CrystEngComm* **2012**, *14*, 1909–1919.
(3) Mastalerz, M. Shape-persistent Organic Cage Compounds by Dynamic Covalent Bond Formation. *Angew. Chem., Int. Ed.* **2010**, *49*, 5042–5053.
(4) Slater, A. G.; Cooper, A. I. Function-led Design of New Porous Materials. *Science* **2015**, *348*, aaa8075.
(5) Tozawa, T.; Jones, J. T. A; Swamy, S. I.; Jiang, S.; Adams, D. J.; Shakespeare, S.; Clowes, R.; Bradshaw, D.; Hasell, T.; Chong, S. Y.; Tang, C.; Thompson, S.; Parker, J.; Trewin, A.; Bacsa, J.; Slawin, A. M. Z.; Steiner, A.; Cooper, A. I. Porous Organic Cages. *Nat. Mater.* **2009**, *8*, 973–978.
(6) Mastalerz, M.; Schneider, M. W.; Oppel, I. M.; Presly, O. A Salicylbisimine Cage Compound with High Surface Area and Selective CO_2/CH_4 Adsorption. *Angew. Chem., Int. Ed.* **2011**, *50*, 1046–1051.
(7) Hong, S.; Rohman, M. R.; Jia, J.; Kim, Y. Y.; Moon, D.; Kim, Y. Y.; Ko, Y. H.; Lee, E.; Kim, K. Porphyrin Boxes: Rationally Designed Porous Organic Cages. *Angew. Chem., Int. Ed.* **2015**, *54*, 13241–13244.
(8) Zhang, G.; Presly, O.; White, F.; Oppel, I. M.; Mastalerz, M. A Permanent Mesoporous Organic Cage with an Exceptionally High Surface Area. *Angew. Chem., Int. Ed.* **2014**, *53*, 1516–1520.
(9) Avellaneda, A.; Valente, P.; Burgun, A.; Evans, J. D.; Markwell-Heys, A. W.; Rankine, D.; Nielsen, D. J.; Hill, M. R.; Sumby, C. J.; Doonan, C. J. Kinetically Controlled Porosity in a Robust Organic Cage Material. *Angew. Chem., Int. Ed.* **2013**, *52*, 3746–3749.
(10) Yaghi, O. M.; Li, H.; Davis, C.; Richardson, D.; Groy, T. L. Synthetic Strategies, Structure Patterns, and Emerging Properties in the Chemistry of Modular Porous Solids. *Acc. Chem. Res.* **1998**, *31*, 474–484.
(11) Côté, A. P.; Benin, A. I.; Ockwig, N. W.; O'Keeffe, M.; Matzger, A. J.; Yaghi, O. M. Porous, Crystalline, Covalent Organic Frameworks. *Science* **2005**, *310*, 1166–1170.
(12) Jiang, J. X.; Su, F.; Trewin, A.; Wood, C. D.; Campbell, N. L.; Niu, H.; Dickinson, C.; Ganin, A. Y.; Rosseinsky, M. J.; Khimyak, Y. Z.; Cooper, A. I. Conjugated Microporous Poly(aryleneethynylene) Networks. *Angew. Chem., Int. Ed.* **2007**, *46*, 8574–8578.
(13) Bushell, A. F.; Budd, P. M.; Attfield, M. P.; Jones, J. T. A.; Hasell, T.; Cooper, A. I.; Bernardo, P.; Bazzarelli, F.; Clarizia, G.; Jansen, J. C. Nanoporous Organic Polymer/Cage Composite Membranes. *Angew. Chem., Int. Ed.* **2013**, *52*, 1253–1256.
(14) Jones, J. T. A.; Hasell, T.; Wu, X.; Bacsa, J.; Jelfs, K. E.; Schmidtmann, M.; Chong, S. Y.; Adams, D. J.; Trewin, A.; Schiffman, F.; Cora, F.; Slater, B.; Steiner, A.; Day, G. M.; Cooper, A. I. Modular

DOI: 10.1021/acscentsci.7b00145
ACS Cent. Sci. XXXX, XXX, XXX–XXX

and Predictable Assembly of Porous Organic Molecular Crystals. *Nature* **2011**, *474*, 367−371.
(15) Hasell, T.; Chong, S. Y.; Schmidtmann, M.; Adams, D. J.; Cooper, A. I. Porous Organic Alloys. *Angew. Chem., Int. Ed.* **2012**, *51*, 7154−7157.
(16) Hasell, T.; Culshaw, J. L.; Chong, S. Y.; Schmidtmann, M.; Little, M. A.; Jelfs, K. E.; Pyzer-Knapp, E. O.; Shepherd, H.; Adams, D. J.; Day, G. M.; Cooper, A. I. Controlling the Crystallization of Porous Organic Cages: Molecular Analogs of Isoreticular Frameworks Using Shape-Specific Directing Solvents. *J. Am. Chem. Soc.* **2014**, *136*, 1438−1448.
(17) Little, M. A.; Chong, S. Y.; Schmidtmann, M.; Hasell, T.; Cooper, A. I. Guest Control of Structure in Porous Organic Cages. *Chem. Commun.* **2014**, *50*, 9465−9468.
(18) Kewley, A.; Stephenson, A.; Chen, L.; Briggs, M. E.; Hasell, T.; Cooper, A. I. *Chem. Mater.* **2015**, *27*, 3207−3210.
(19) Chen, L.; Reiss, P. S.; Chong, S. Y.; Holden, D.; Jelfs, K. E.; Hasell, T.; Little, M. A.; Kewley, A.; Briggs, M. E.; Stephenson, A.; Thomas, K. M.; Armstrong, J. a; Bell, J.; Busto, J.; Noel, R.; Liu, J.; Strachan, D. M.; Thallapally, P. K.; Cooper, A. I. Separation of Rare Gases and Chiral Molecules by Selective Binding in Porous Organic Cages. *Nat. Mater.* **2014**, *13*, 954−960.
(20) Mitra, T.; Jelfs, K. E.; Schmidtmann, M.; Ahmed, A.; Chong, S. Y.; Adams, D. J.; Cooper, A. I. Molecular Shape Sorting Using Molecular Organic Cages. *Nat. Chem.* **2013**, *5*, 276−281.
(21) Cai, J.; Xing, Y.; Zhao, X. Quantum Sieving: Feasibility and Challenges for the Separation of Hydrogen Isotopes in Nanoporous Materials. *RSC Adv.* **2012**, *2*, 8579−8586.
(22) Kowalczyk, P.; Terzyk, A. P.; Gauden, P. A.; Furmaniak, S.; Pantatosaki, E.; Papadopoulos, G. K. Intrinsic D_2/H_2 Selectivity of NaX Zeolite: Interplay between Adsorption and Kinetic Factors. *J. Phys. Chem. C* **2015**, *119*, 15373−15380.
(23) Niimura, S.; Fujimori, T.; Minami, D.; Hattori, Y.; Abrams, L.; Corbin, D.; Hata, K.; Kaneko, K. Dynamic Quantum Molecular Sieving Separation of D_2 from H_2−D_2 Mixture with Nanoporous Materials. *J. Am. Chem. Soc.* **2012**, *134*, 18483−18486.
(24) Oh, H.; Hirscher, M. Quantum Sieving for Separation of Hydrogen Isotopes Using MOFs. *Eur. J. Inorg. Chem.* **2016**, *2016*, 4278−4289.
(25) Tilford, R. W.; Mugavero, S. J.; Pellechia, P. J.; Lavigne, J. Tailoring Microporosity in Covalent Organic Frameworks. *Adv. Mater.* **2008**, *20*, 2741−2746.
(26) Wang, Y.; Tan, C.; Sun, Z.; Xue, Z.; Zhu, Q.; Shen, C.; Wen, Y.; Hu, S.; Wang, Y.; Sheng, T.; Wu, X. Effect of Functionalized Groups on Gas-Adsorption Properties: Syntheses of Functionalized Microporous Metal−Organic Frameworks and Their High Gas-Storage Capacity. *Chem. - Eur. J.* **2014**, *20*, 1341−1348.
(27) Bhattacharya, B.; Haldar, R.; Dey, R.; Maji, T. K.; Ghoshal, D. Porous Coordination Polymers Based on Functionalized Schiff Base Linkers: Enhanced CO_2 Uptake by Pore Surface Modification. *Dalton Trans.* **2014**, *43*, 2272−2282.
(28) Schneider, M. W.; Oppel, I. M.; Ott, H.; Lechner, L. G.; Hauswald, H. J. S.; Stoll, R.; Mastalerz, M. Periphery-Substituted [4 + 6] Salicylbisimine Cage Compounds with Exceptionally High Surface Areas: Influence of the Molecular Structure on Nitrogen Sorption Properties. *Chem. - Eur. J.* **2012**, *18*, 836−847.
(29) Pyzer-Knapp, E. O.; Thompson, H. P. G.; Schiffmann, F.; Jelfs, K. E.; Chong, S. Y.; Little, M. a.; Cooper, A. I.; Day, G. M. Predicted Crystal Energy Landscapes of Porous Organic Cages. *Chem. Sci.* **2014**, *5*, 2235−2245.
(30) Eddaoudi, M.; Kim, J.; Rosi, N.; Vodak, D.; Wachter, J.; O'Keeffe, M.; Yaghi, O. M. Systematic Design of Pore Size and Functionality in Isoreticular MOFs and Their Application in Methane Storage. *Science* **2002**, *295*, 469−472.
(31) Hass, H. B.; Bender, M. L. *o*-Tolualdehyde. *Org. Synth.* **1950**, *30*, 99.
(32) Jiang, S.; Jones, J. T. A; Hasell, T.; Blythe, C. E.; Adams, D. J.; Trewin, A.; Cooper, A. I. Porous Organic Molecular Solids by Dynamic Covalent Scrambling. *Nat. Commun.* **2011**, *2*, 207.
(33) Briggs, M. E.; Slater, A. G.; Lunt, N.; Jiang, S.; Little, M. A.; Greenaway, R. L.; Hasell, T.; Battilocchio, C.; Ley, S. V.; Cooper, A. I. Dynamic Flow Synthesis of Porous Organic Cages. *Chem. Commun.* **2015**, *51*, 17390−17393.
(34) Pulido, A.; Chen, L.; Kaczorowski, T.; Holden, D.; Little, M. A.; Chong, S. Y.; Slater, B. J.; McMahon, D. P.; Bonillo, B.; Stackhouse, C. J.; Stephenson, A.; Kane, C. M.; Clowes, R.; Hasell, T.; Cooper, A. I.; Day, G. M. Functional Materials Discovery Using Energy−Structure−Function Maps. *Nature* **2017**, *543*, 657−664.
(35) Frisch, M. J.; Trucks, G. W.; Schlegel, H. B.; Scuseria, G. E.; Robb, M. A.; Cheeseman, J. R.; Scalmani, G.; Barone, V.; Mennucci, B.; Petersson, G. A.; Nakatsuji, H.; Caricato, M.; Li, X.; Hratchian, H. P.; Izmaylov, A. F.; Bloino, J.; Zheng, G.; Sonnenberg, J. L.; Hada, M.; Ehara, M.; Toyota, K.; Fukuda, R.; Hasegawa, J.; Ishida, M.; Nakajima, T.; Honda, Y.; Kitao, O.; Nakai, H.; Vreven, T.; Montgomery, J. A., Jr.; Peralta, J. E.; Ogliaro, F.; Bearpark, M.; Heyd, J. J.; Brothers, E.; Kudin, K. N.; Staroverov, V. N.; Kobayashi, R.; Normand, J.; Raghavachari, K.; Rendell, A.; Burant, J. C.; Iyengar, S. S.; Tomasi, J.; Cossi, M.; Rega, N.; Millam, J. M.; Klene, M.; Knox, J. E.; Cross, J. B.; Bakken, V.; Adamo, C.; Jaramillo, J.; Gomperts, R.; Stratmann, R. E.; Yazyev, O.; Austin, A. J.; Cammi, R.; Pomelli, C.; Ochterski, J. W.; Martin, R. L.; Morokuma, K.; Zakrzewski, V. G.; Voth, G. A.; Salvador, P.; Dannenberg, J. J.; Dapprich, S.; Daniels, A. D.; Farkas, Ö.; Foresman, J. B.; Ortiz, J. V.; Cioslowski, J.; Fox, D. J. *Gaussian 09, Revision D.01*; Gaussian, Inc.: Wallingford, CT, 2009.
(36) Price, S. L.; Leslie, M.; Welch, G. W. A.; Habgood, M.; Price, L. S.; Karamertzanis, P. G.; Day, G. M. Modelling Organic Crystal Structures Using Distributed Multipole and Polarizability-based Model Intermolecular Potentials. *Phys. Chem. Chem. Phys.* **2010**, *12*, 8478−8490.
(37) Cruz-Cabeza, A. J.; Day, G. M.; Jones, W. Predicting Inclusion Behaviour and Framework Structures in Organic Crystals. *Chem. - Eur. J.* **2009**, *15*, 13033−13040.
(38) Holden, D.; Jelfs, K. E.; Cooper, A. I.; Trewin, A.; Willock, D. J. Bespoke Force Field for Simulating the Molecular Dynamics of Porous Organic Cages. *J. Phys. Chem. C* **2012**, *116*, 16639−16651.
(39) Camp, J. S.; Sholl, D. S. Transition State Theory Methods To Measure Diffusion in Flexible Nanoporous Materials: Application to a Porous Organic Cage Crystal. *J. Phys. Chem. C* **2016**, *120*, 1110−1120.
(40) Evans, J. D.; Huang, D. M.; Hill, M. R.; Sumby, C. J.; Thornton, A. W.; Doonan, C. J. Feasibility of Mixed Matrix Membrane Gas Separations Employing Porous Organic Cages. *J. Phys. Chem. C* **2014**, *118*, 1523−1529.
(41) Hasell, T.; Miklitz, M.; Stephenson, A.; Little, M. A.; Chong, S. Y.; Clowes, R.; Chen, L.; Holden, D.; Tribello, G. A.; Jelfs, K. E.; Cooper, A. I. Porous Organic Cages for Sulfur Hexafluoride Separation. *J. Am. Chem. Soc.* **2016**, *138*, 1653−1659.
(42) Holden, D.; Chong, S. Y.; Chen, L.; Jelfs, K. E.; Hasell, T.; Cooper, A. I. Understanding Static, Dynamic and Cooperative Porosity in Molecular Materials. *Chem. Sci.* **2016**, *7*, 4875−4879.
(43) Fairen-Jimenez, D.; Moggach, S. A.; Wharmby, M. T.; Wright, P. A.; Parsons, S.; Düren, T. Opening the Gate: Framework Flexibility in ZIF-8 Explored by Experiments and Simulations. *J. Am. Chem. Soc.* **2011**, *133*, 8900−8902.
(44) Liu, J.; Thallapally, P. K.; Strachan, D. Metal−Organic Frameworks for Removal of Xe and Kr from Nuclear Fuel Reprocessing Plants. *Langmuir* **2012**, *28*, 11584−11589.
(45) Bojdys, M. J.; Briggs, M. E.; Jones, J. T. A.; Adams, D. J.; Chong, S. Y.; Schmidtmann, M.; Cooper, A. I. Supramolecular Engineering of Intrinsic and Extrinsic Porosity in Covalent Organic Cages. *J. Am. Chem. Soc.* **2011**, *133*, 16566−16571.

DOI: 10.1021/acscentsci.7b00145
ACS Cent. Sci. XXXX, XXX, XXX−XXX